Independent control of polar and azimuthal anchoring

ANQUETIL-DECK, C., CLEAVER, Doug <http://orcid.org/0000-0002-4278-0098>, BRAMBLE, J. P. and ATHERTON, T. J.

Published version

ANQUETIL-DECK, C., CLEAVER, Doug, BRAMBLE, J. P. and ATHERTON, T. J. (2013). Independent control of polar and azimuthal anchoring. Physical review E. Statistical, nonlinear and soft matter physics, 88 (1), 012501-1-012501-10.

Independent control of polar and azimuthal anchoring

C. Anquetil-Deck* and D. J. Cleaver†
Materials and Engineering Research Institute, Sheffield Hallam University, City Campus, Howard Street, Sheffield, S1 1WB,UK

J. P. Bramble
School of Physics and Astronomy, University of Leeds, Woodhouse Lane, Leeds, LS2 9JT, UK

T. J. Atherton
Department of Physics and Astronomy, Center for Nanoscopic Physics, Tufts University, Medford, Massachusetts 02155, USA
(Received 24 April 2013; published 1 July 2013)

Monte Carlo simulation, experiment, and continuum theory are used to examine the anchoring exhibited by a nematic liquid crystal at a patterned substrate comprising a periodic array of rectangles that, respectively, promote vertical and planar alignment. It is shown that the easy axis and effective anchoring energy promoted by such surfaces can be readily controlled by adjusting the design of the pattern. The calculations reveal rich behavior: for strong anchoring, as exhibited by the simulated system, for rectangle ratios $\geqslant 2$ the nematic aligns in the direction of the long edge of the rectangles, the azimuthal anchoring coefficient changing with pattern shape. In weak anchoring scenarios, however, including our experimental systems, preferential anchoring is degenerate between the two rectangle diagonals. Bistability between diagonally aligned and edge-aligned arrangement is predicted for intermediate combinations of anchoring coefficient and system length scale.

DOI: 10.1103/PhysRevE.88.012501 PACS number(s): 61.30.Hn, 61.30.Dk, 07.05.Tp

I. INTRODUCTION

Conventional uniform surface treatments for confined nematic liquid crystals (LCs), such as rubbed or photoaligned polymers, are limited to a narrow specification: they typically promote vertical or planar alignment where both the preferred orientation and associated anchoring energy are difficult to alter. In contrast, topographically or chemically patterned surfaces permit essentially arbitrary control of the easy axis and anchoring potential through appropriate adjustment of the pattern features [1]; suitable patterning techniques include atomic force microscope scribing of polymer films [2,3], microcontact printing of self-assembled monolayers (SAMs) [4–6], and photolithography [7–10]. By imprinting a design of appropriate symmetry, it is also possible to pattern a surface to promote more than one stable alignment orientation [2,11–14] thus enabling the fabrication of bistable devices [2,10,15–18]. Very recently SAM-patterned substrates have been used to achieve rapid switching [19].

The purpose of the present paper is to investigate the alignment behavior of a nematic confined by patterned surfaces decorated with a stretched-chessboard-like array of rectangles that alternately promote planar and vertical alignment. This arrangement is of interest since it is intermediate between arrays of stripes and squares, patterns which have previously been shown to promote qualitatively different anchoring behaviors.

For striped systems, it was found experimentally by Lee and Clark [11] that the polar orientation of the bulk nematic depends on the relative widths of the vertical- and planar-promoting stripes while the azimuthal alignment consistently lies along the lengths of the stripes. It was proposed that the latter was due to elastic anisotropy, i.e., the differing energetic costs of various symmetries of bulk orientational deformation. Calculations using continuum theory [20,21] and Monte Carlo (MC) simulation of hard particles [22] affirmed this notion and showed that it held across the very different length scales over which these two theoretical techniques apply. Further, it was shown that by adjusting the relative stripe width and cell thickness, the polar anchoring angle could be altered continuously from planar to vertical [21,23]. Despite the apparent simplicity of the striped pattern, in some scenarios its phase behavior is further enriched: if two striped substrates sandwich a cell that is only a few molecular lengths thick, the nematic may form separate vertical and planar domains "bridging" the film [23]. Alternatively, if some of the stripes are sufficiently narrow, the pattern is neglected by the structure within the nematic [24,25].

As expected from symmetry [2,12], degenerate alignment is observed for systems comprising chessboard-like arrangements of squares promoting competing alignments. Experimental studies on SAM-based square-patterned systems have shown that, for feature sizes of $\simeq 30\ \mu$m, the favored alignment runs along the diagonals of the planar-promoting squares [22]. When the patterning length scale is reduced to that accessible to particle-based simulation, however, the preferred orientations run along the pairs of opposite edges of the squares [26]. An anchoring transition between these arrangements is then predicted for, e.g., a sufficiently weak polar anchoring condition. Unlike the striped systems, however, no "bridging" behavior has been observed for square-patterned systems, even for very thin films.

Here we investigate the way in which the strong azimuthal coupling and variable polar anchoring associated with nematics on striped substrates segues into the anchoring transition

*Present address: Karlsruhe Institute of Technology, Institute for Meteorology and Climate Research, Atmospheric Aerosol Research Department (IMK-AAF), Hermann-von-Helmholtz-Platz 1, D-76344 Eggenstein-Leopoldshafen Germany.
†d.j.cleaver@shu.ac.uk

found for square-patterned substrates. We do this by studying the polar and azimuthal anchoring behaviors accessible to substrate patternings based on rectangles of adjustable length-scale and aspect ratio. This is achieved through a combination of molecular-level MC simulation, experiment, and continuum theory. The paper is organized as follows: the MC simulation methodology is described in Sec. II, and associated results are presented in Sec. III. Some preliminary experimental results are then given in Sec. IV, and a continuum calculation is performed and used to reconcile the preceding results in Sec. V. Conclusions are drawn in Sec. VI.

II. MONTE CARLO MODEL AND SIMULATION DETAILS

To initiate this study, we have performed a series of MC simulations of rod-shaped particles confined in slab geometry between two planar walls. The model used is essentially that described in Ref. [26]. Briefly, interparticle interactions have been modeled through the hard Gaussian overlap (HGO) potential [27], which can be seen as equivalent to the well-known Gay-Berne model [28], stripped of its attractive interaction. The particle-substrate interactions have been modeled using the hard needle-wall potential (HNW) [29] where a hard axial needle of length $\sigma_0 k_s$ is placed at the center of each particle (see Fig. 1). The parameter k_s provides a molecular-level control on the surface anchoring properties. The results presented in Secs. III A and III B have been obtained for systems of 864 HGO particles of length to breadth ratio $\kappa = 3$, confined between two rectangle-patterned substrates. The substrates were separated by a distance $L_z = 4\kappa\sigma_0$, where σ_0 is the particle diameter, periodic boundary conditions being imposed in the x and y directions.

On each substrate, k_s was set to a vertical-aligning value ($k_s \leqslant 1.0$) for a portion of its area and a planar value ($k_s \geqslant 2.0$) for the remainder, and sharp boundaries were imposed between the competing alignment regions. The patterns on the top and bottom surfaces have been kept in perfect registry with one another, as shown in the schematic in Fig. 2.

Each system has been initialized at low density and gently compressed by decreasing the box dimensions L_x and L_y while keeping the substrate separation L_z and the rectangular ratio $R = L_x/L_y$ fixed. At each density, run lengths of 1 million MC sweeps (where one sweep represents one attempted move per particle) were performed, averages and profiles being accumulated for the final 500 000 sweeps.

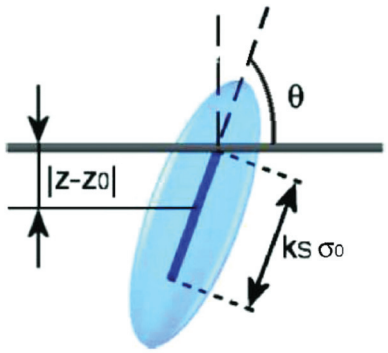

FIG. 1. (Color online) Schematic representation of the geometry used for the hard needle-wall (HNW) particle-substrate interaction [29].

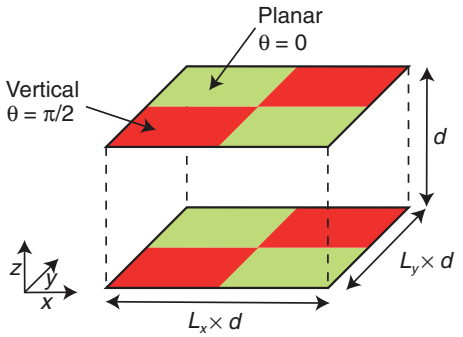

FIG. 2. (Color online) Schematic representation of rectangle patterned systems tiled with vertical-inducing (red/dark) and planar-inducing (green/light) substrate regions. The azimuthal angle ϕ is zero along the x axis.

Analysis has been performed by dividing stored system configurations into 100 equidistant constant-z slices and performing averages of relevant observables in each slice. This yields profiles of quantities such as number density, $\rho^*(z)$, from which structural changes can be assessed. Orientational order profiles have also been calculated, particularly

$$Q_{zz}(z) = \frac{1}{N(z)} \sum_{i=1}^{N(z)} \left(\frac{3}{2} u_{i,z}^2 - \frac{1}{2} \right), \tag{1}$$

which measures variation across the confined films of orientational order measured with respect to the substrate normal. Here $N(z)$ is the instantaneous occupancy of the relevant slice. We have also further subdivided the system to assess lateral inhomogeneities induced by the patterning. Specifically, we have computed profiles corresponding to particles residing between the vertical-aligning and planar-aligning substrate regions.

III. SIMULATION RESULTS

A. Influence of the surface interaction parameter

In this section we assess the influence of microscopic rectangular patterning on the structure and anchoring of a confined LC film. To this end, we present results obtained from full compression sequences of MC simulations performed on a series of systems with differing pairs of surface interaction parameters. For reasons of space we show data only for high-density ($\rho = 0.4$) systems and concentrate on the influence of the substrate parameters.

We initially consider systems for which the rectangular ratio $R = 3$. We first used a combination of strong planar alignment of the molecules on the substrate ($k_s = 3$) with a strong vertical alignment ($k_s = 0$). Then we slightly weakened the vertical alignment ($k_s = 0.5$) before going on to use a weak vertical alignment ($k_s = 1$). The high-density snapshots corresponding to such systems are represented in Fig. 3. These clearly indicate that, for all combinations of k_s values, these systems exhibited a central ordered monodomain at high density. From these snapshots it is apparent that the monodomains

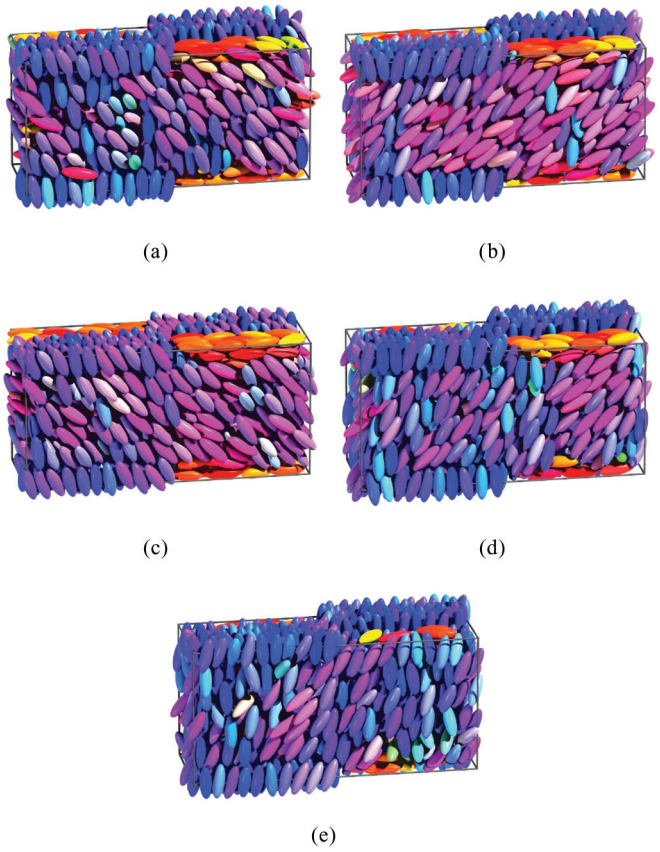

FIG. 3. (Color online) Snapshots of system with $L_x = 3L_y$ and different combinations of planar and vertical k_s values. (a) $k_s = 0.5$, $k_s = 3$; (b) $k_s = 0$, $k_s = 3$; (c) $k_s = 1$, $k_s = 3$; (d) $k_s = 0$, $k_s = 2.5$; (e) $k_s = 0$, $k_s = 2$.

were all aligned in the x-z plane. This is consistent with what was observed for equivalent stripe-patterned systems [23]. It suggests, then, that for an edge ratio of 3, rectangle patterned substrates act rather like well defined stripes, i.e., that it is straightforward to pin the azimuthal angle using the shape asymmetry of rectangular substrate patterns. The second item of note from these snapshots is that the surface patterns do not "bridge" across the film. As with square patterns [26], this is presumably due to the different interfacial stabilities that would pertain at the resultant twistlike and bendlike domain boundaries.

To substantiate this assessment, we plot in Fig. 4 the corresponding Q_{zz} profiles to quantify the differences between these three systems with strong planar anchoring (i.e., $k_s = 3$). From these it is apparent that in the vertical regions, the Q_{zz} value is slightly greater for strong vertical parametrizations [see Fig. 4(a)]. This difference is not apparent, though, in the planar regions [see Fig. 4(b)]. Because of the small differences in these graphs, we have also calculated the average bulk tilt angles θ_z. These are presented in Table I and confirm that these systems exhibit very similar tilt angles in the differently anchored regions, typical variations being only 7° within each system. These modest variations correspond to nematic monodomains with small undulations of the polar anchoring orientation. As expected, on decreasing the strength of the vertical anchoring at the surface, the bulk alignment becomes

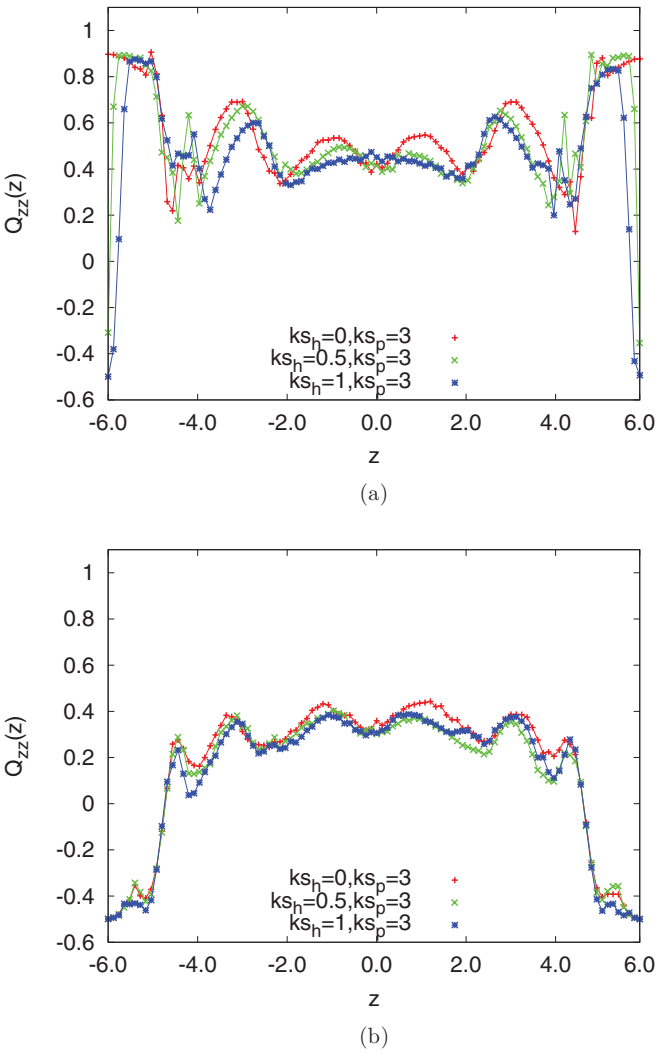

FIG. 4. (Color online) Influence of k_s on the $\rho = 0.4$ Q_{zz} profiles for the differently anchored subsystems with rectangle ratio $R = 3$ and strong planar anchoring (a) between vertically aligned substrate regions, (b) between planar-aligned substrate regions.

increasingly planar: the tabulated values for θ_z decrease with increase in the vertical-region k_s value. While this variation is very weak, the presence of the vertical-aligning surface

TABLE I. Average tilt angle, by surface region, for different rectangle ratios L_x/L_y and substrate couplings k_s.

	Planar		Vertical	
L_x/L_y	k_s	$\theta_z(^\circ)$	k_s	$\theta_z(^\circ)$
3	3	53	0	59
3	3	50	0.5	57
3	3	50	1	56
3	2.5	60	0	64
3	2	65	0	68
2	3	55	0	61
2	3	54	0.5	59
2	3	45	1	50
2	2.5	61	0	66
2	2	75	0	75

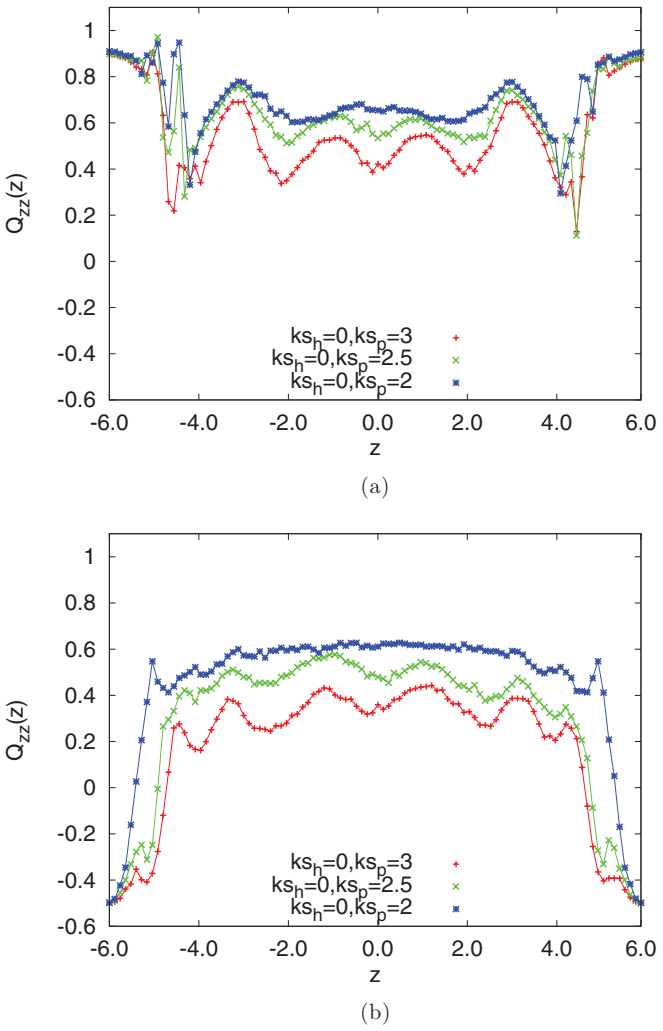

FIG. 5. (Color online) Influence of k_s on the $\rho = 0.4$ Q_{zz} profiles for the differently anchored subsystems with rectangle ratio $R = 3$ and strong vertical anchoring (a) between vertically aligned substrate regions, (b) between planar-aligned substrate regions.

regions is substantial; the measured tilt angles are far from 0°, which would be seen in the absence of these vertical-aligning substrate regions.

We next consider the influence of the strength of the planar anchoring regions in the presence of strong vertical anchoring regions. This is achieved by simulating $k_s = 0$ regions combined with strong planar ($k_s = 3$), moderate planar ($k_s = 2.5$), and weak planar ($k_s = 2$) regions, respectively. From the variation of the corresponding Q_{zz} profiles (see Fig. 5), it is apparent that decreasing the planar anchoring strength causes the Q_{zz} profiles to become more positive throughout the confined film. As confirmed by the snapshots (Fig. 3) and the corresponding tilt angle data in Table I, this means that the central domains become increasingly aligned perpendicular to the surfaces. Again, this makes intuitive sense, since the relative influence of the vertical anchoring contribution would be expected to grow in such circumstances. The bulk tilt angle is, though, more sensitive here to change of the planar-region coupling parameter than it was previously to change of the vertical-region coupling parameter.

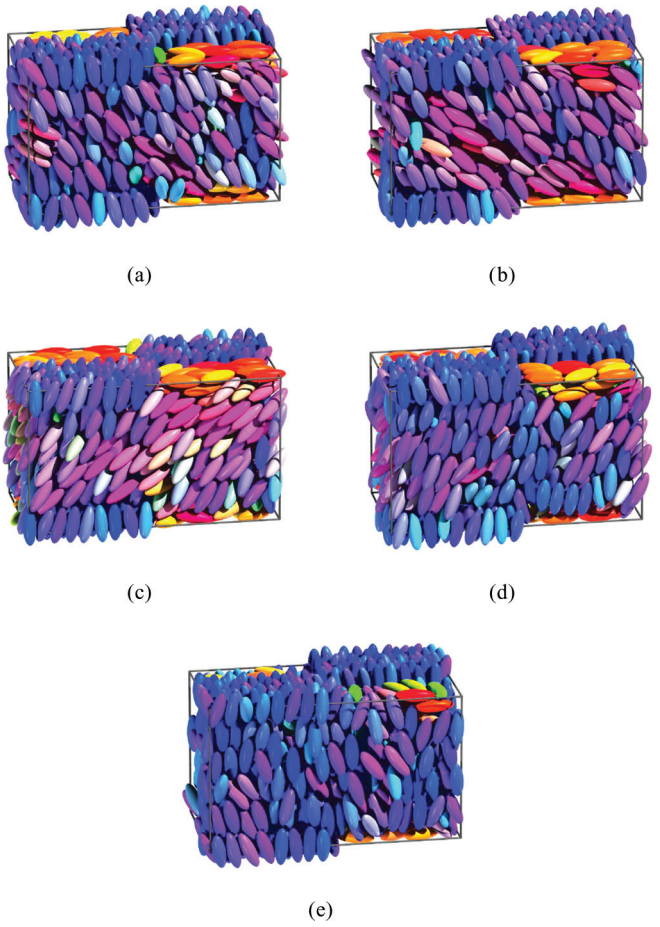

FIG. 6. (Color online) Snapshots of system with $L_x = 2L_y$ and different combinations of planar and vertical k_s values. Strong vertical anchoring. (a) $k_s = 0, k_s = 3$; (b) $k_s = 0.5, k_s = 3$; (c) $k_s = 1, k_s = 3$; (d) $k_s = 0$, $k_s = 2.5$; (e) $k_s = 0$, $k_s = 2$.

B. Influence of the rectangle ratio $R = L_x/L_y$

In order to assess the influence of the rectangle ratio on these small length-scale systems, an equivalent series of simulations has been performed on systems patterned with $R = L_x/L_y$=2 substrate rectangles. Corresponding high-density snapshots are represented in Fig. 6. We note from these that again, in all cases, the induced anchoring lies in the x-z plane. This indicates that fixing the azimuthal angle to coincide with the long edge of the rectangle patterns is achievable even with $R \simeq 2$. The influence of the ratio R on the azimuthal angle will be investigated in more detail later in the paper.

Figure 7 shows the high-density Q_{zz} profiles of $R = 2$ systems with strong planar anchoring regions and varying vertical anchoring strength. These profiles are more sensitive to the variation of the vertical surface anchoring parameter than the corresponding $R = 3$ were. Specifically, while the $R = 2$ Q_{zz} profiles are similar for $k_s = 0$ and $k_s = 0.5$, significantly lower Q_{zz} values were found in the central region of the $k_s = 1$ film. The corresponding tilt angle shifts are reported in Table I. Figure 8 shows the influence of the planar k_s parameter on $R = 2$ systems with strong vertically aligned regions. Here the Q_{zz} values are strongly influenced by the planar k_s values,

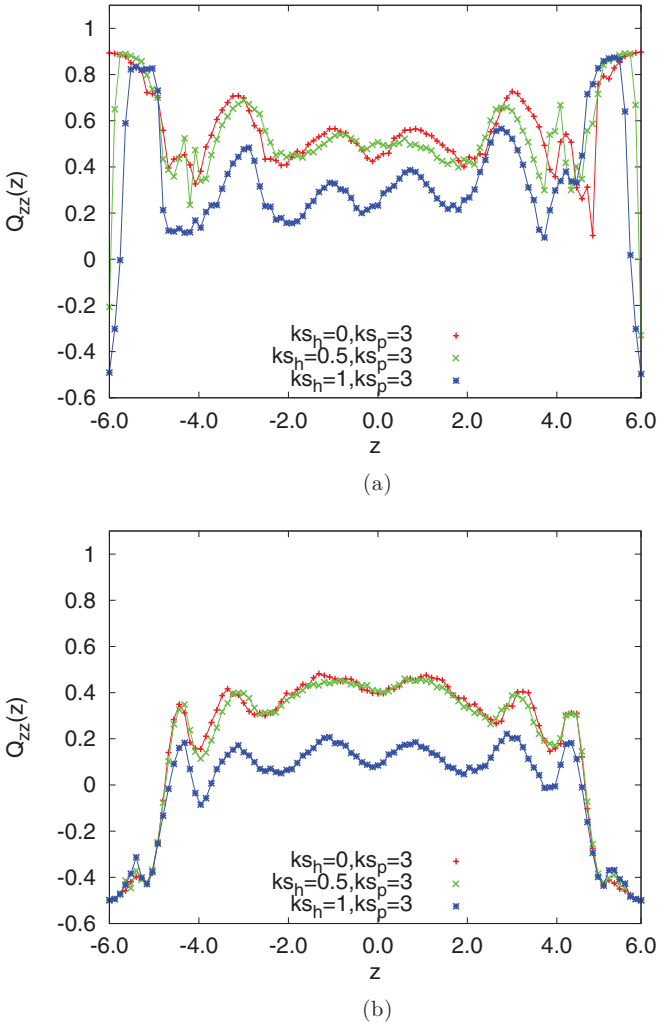

FIG. 7. (Color online) Influence of k_s on the $\rho = 0.4$ Q_{zz} profiles for the differently anchored subsystems with rectangle ratio $R = 2$ and strong planar anchoring (a) between vertically aligned substrate regions, (b) between planar-aligned substrate regions.

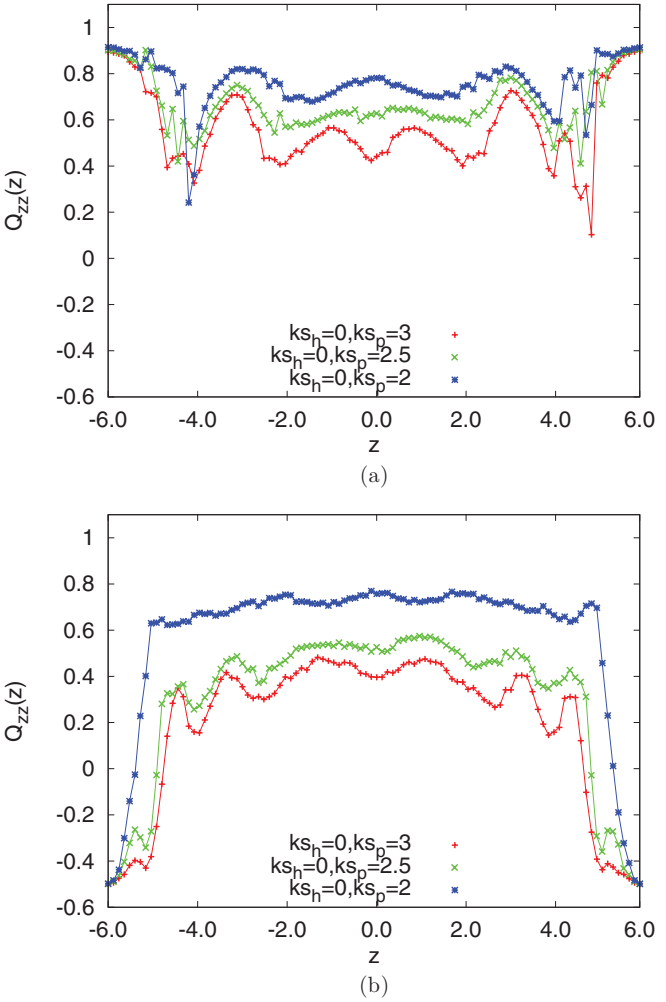

FIG. 8. (Color online) Influence of k_s on the $\rho = 0.4$ Q_{zz} profiles for the differently anchored subsystems with rectangle ratio $R = 2$ and strong vertical anchoring (a) between vertically aligned substrate regions, (b) between planar-aligned substrate regions.

both regions showing increase in Q_{zz} as the planar anchoring component is weakened. This corresponds to the particles lying increasingly normal to the surfaces, as confirmed by the data given in Table I.

While the qualitative behaviors of the $R = 2$ and $R = 3$ systems simulated here were very similar, some quantitative differences were determined. From the data reported in Table I, increase in L_x/L_y was generally associated with a decrease in the tilt angles adopted in both substrate regions. The one exception to this was the substrate combination $k_s = 1, k_s = 3$ identified above as displaying strong planar character for $R = 2$. A further observation is that the sensitivity of tilt angle to substrate conditions was consistently greater for the $R = 2$ systems than the $R = 3$. It is not appropriate to examine this tilt variation with shape up to the $R = \text{inf}$ limit because such systems exhibit domain bridging rather than a tilted monodomain [23].

Finally, we assess the effect of the rectangle ratio on the preferred azimuthal angle. In Ref. [26], we saw that the azimuthal angle cannot be effectively controlled using square-patterned substrates, degenerate alignment being seen between the two edge directions. Here, though, for both R values investigated, clear orientational pinning was apparent. In order to gauge the strength of this pinning, we plot, in Fig. 9, azimuthal angle distributions for substrate-region particles on the different pattern types. This confirms a strong departure from the degenerate behavior seen for square patterns. For $R = 2$, while a small but distinct subset of particles aligned along the short rectangle edge, long-edge alignment was dominant. This effect was even more marked for $R = 3$ and, indeed, was essentially as strong as that seen for full stripe patterning.

IV. EXPERIMENT

To determine the effect of rectangular substrate patterning at larger length scales, a set of experimental cells was prepared using the microcontact printing technique described in Ref. [22]. In these, SAMs of -COOH and -CF_3 terminated alkanethiols were used to promote planar and vertical

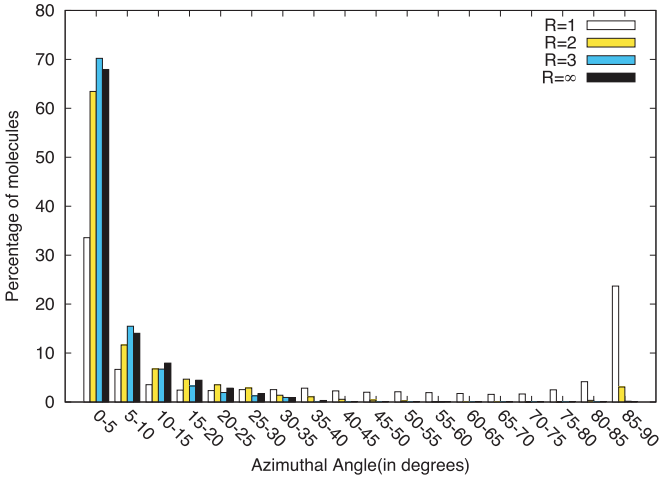

FIG. 9. (Online color) Influence of the pattern anisotropy on the azimuthal angle distribution of near-substrate particles for systems with $k_s = 0$ and $k_s = 3$.

alignment, respectively, in the different pattern regions. Unlike the simulated systems, however, only one patterned substrate was used in these cells; the second substrate was always prepared with a uniform vertical-aligning treatment. We do not expect the uniform vertical surface to significantly change the azimuthal alignment since the MC simulations show that the elastic distortion is strongly confined to the surface in these systems. Moreover, the uniform vertical treatment for symmetry reasons cannot itself favor any particular azimuthal orientation. Consequently, these cells comprised both vertical-vertical (VV) and planar-vertical (PV) subregions. The cells were prepared with a nominal thickness 23μm, filled with the nematic material 9CB in the isotropic phase and cooled into the nematic phase while being observed with a polarizing microscope.

Figure 10 shows a polarizing microscopy image of a typical cell, one surface of which was patterned with squares of 8 μm width (i.e., a 16 μm period). For this system, the maximum transmission in the planar regions occurred when the checkerboard was orientated parallel to the polarizers.

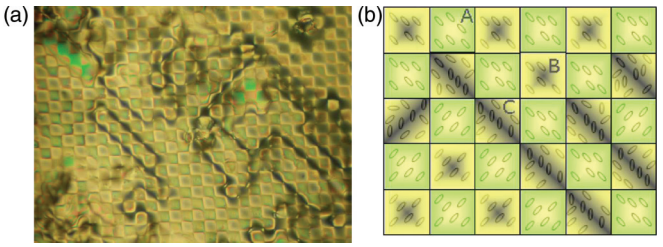

FIG. 10. (Color online) (a) Polarizing microscopy image of 9CB aligned by a COOH/CF3 SAM patterned with a checkerboard with squares of width 8 μm. The polarizers and analyzers are crossed and are parallel to the checkerboard. (b) Schematic showing the bulk director orientation on a square-patterned substrate. A: PV region, B: VV region with identical neighbors, C: VV region with different neighboring PV regions. Note the direction of the LC director in a VV region tries to match that of its neighbors.

From this, we deduce that the director had a component aligned diagonally across the planar-aligned squares. There are two different degenerate states for this, corresponding to the two opposite diagonals, which are optically identical. Nonetheless, optical consequences of splay and twist in the VV regions reveal where boundaries between the differently oriented PV domains lie: at an interface between these two the azimuthal angle ϕ rotates gradually by $\pi/2$ from one side to the other, so along the diagonal of the square, ϕ averages to be parallel to one of the polarizer directions and hence appears dark. The VV regions are splayed and twisted in the bulk of the cell due to their requirement to accommodate the splayed state in the neighboring PV regions. When a VV region is surrounded by four PV regions of the same hybrid aligned nematic (HAN) configuration, its director points in the same diagonal plane as do those of its neighbors. However, when it is surrounded by PV regions with differing HAN configurations, the VV region is not able to match its boundary requirements with a simple HAN profile. Instead, a twist component develops, which can been seen optically as a darker VV square. As these dark VV squares only arise where there are neighbors with different PV region alignments, they form a border around domains of the degenerate HAN states. This figure shows as well a schematic illustrating these different states and their relationship to the microscopy image. This diagonal alignment behavior in VV regions is predicted by continuum model calculations [26] if the polar anchoring energy promoted by the surface is rather weak.

A second set of cells was prepared with rectangular patterns of different aspect ratios; otherwise, parameters and conditions were equivalent to those used for the square-patterned cell. Microscopy images are shown in Fig. 11(a) and 11(b) and the measured azimuthal alignment angles are displayed in Table II; these were obtained as for the square pattern by rotating the sample under the microscope so as to maximize the extinction between crossed polarizers.

When the symmetry of square checkerboards was broken in this way, a number of alignment changes were observed. We still have two degenerate azimuthal states seen for the regular squares, but the azimuthal orientation in the center is no longer at 45°. On rotation between crossed polarizers, dark states were observed for anticlockwise (negative) and clockwise (positive) rotations. Defining a positive angle ϕ from the long axis of the rectangle, dark states occur at rotations of $-\phi^\circ$, $90-\phi^\circ$ for one state (ϕ) and $-(90-\phi)^\circ$, $90+\phi^\circ$ for the other state ($-\phi$). However optical degeneracy also has to be considered, as the same configurations could be equally explained by azimuthal angles of $90-\phi^\circ$ and $-(90-\phi)^\circ$. Here we use the fact that, when observing with parallel polarizers set horizontally, there is no contrast between the PV regions and VV regions if the horizontal components of refractive index in the HAN and vertical states are equal. This allows us to correctly identify the azimuthal angles. Optical compensators or direct imaging with fluorescent confocal polarizing microscopy (FCPM) could also be used to distinguish between these optically degenerate states.

For an aspect ratio of 1.2, the director is at 40° measured from the vertical. Dark states can be seen on clockwise rotation to 40° and anticlockwise rotation to 50°, the latter

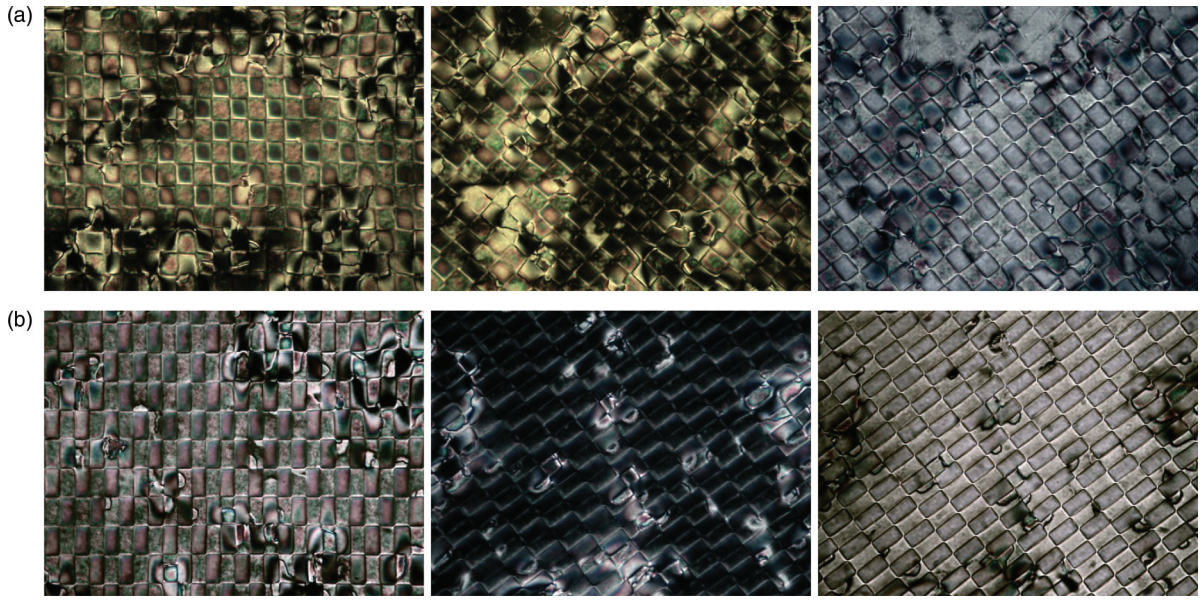

FIG. 11. (Color online) Polarizing microscopy images of 9CB on a rectangular patterned surface. (a) PM images of 9CB aligned on a COOH/CF_3 SAM patterned with a checkerboard of rectangles, a = 20 μm, b = 24 μm. (1) A uniform region of interest, (2) 50° anticlockwise sample rotation with crossed polarizers, (3) 50° anticlockwise sample rotation with parallel polarizers aligned horizontally. (b) PM images of 9CB aligned on a COOH/CF_3 SAM patterned with a checkerboard of rectangles, a = 20 μm and b = 40 μm. (1) A uniform region of interest, (2) 53° clockwise sample rotation with crossed polarizers, (3) 53° clockwise rotation with parallel polarizers aligned horizontally.

shown in Fig. 11(a)(2). Parallel polarizer images also show the difference between the bistable states 11(a)(3). The extinction angle is intriguingly close to arctan(1/1.2) = 39.8°, the angle of the director if pointing from the center of the rectangle to a corner. Additional states are also observed, as shown in Fig. 11(a)(3), there are regions where the director is parallel to the long axis of the rectangle. These regions have a bright state on rotation to 45° between crossed polarizers. Patterns with an increasing ratio up to 2 were printed, the final example of which can be seen in Fig. 11(b) with similar behavior to the aspect ratio 1.2 case. The observed alignment angles are summarized in Table II. Although the MC simulation predicts a different alignment direction to that observed experimentally, there is a qualitative agreement between the two in that the tendency of the nematic is to align with the longer side of the rectangle with increasing aspect ratio.

TABLE II. Observed alignment of 9CB on rectangle patterned surfaces.

Width (μm)	length (μm)	Aspect ratio	Azimuthal angle from long axis (°)
20	20	1	45
20	24	1.2	40
20	28	1.4	36
20	32	1.6	32
20	36	1.8	29
20	40	2	27

V. CONTINUUM MODEL

To reconcile the apparently contradictory observations from our MC simulations and experiments, we now examine the rectangle pattern using a continuum theory approach following the procedure described in our previous paper [26]. Our objective is to determine the director field

$$\hat{\mathbf{n}}(\vec{x}) = (\cos\theta \sin\phi, \cos\theta \cos\phi, \sin\theta) \tag{2}$$

that minimizes the free energy consisting of the Frank energy and the surface energy

$$F = \frac{1}{2}\int d^3x\ K_1 (\nabla \cdot \hat{\mathbf{n}})^2 + K_2[\hat{\mathbf{n}} \cdot (\nabla \times \hat{\mathbf{n}})]^2 + K_3 |\hat{\mathbf{n}} \times (\nabla \times \hat{\mathbf{n}})|^2 + \int_s \mathrm{d}S\ g(\vec{\mathbf{n}},\vec{\mathbf{n}}_0) \tag{3}$$

within two simplifying assumptions: that $K_1 = K_3 \neq K_2$ with $\tau = K_2/K_1$ and also that only variations in θ are considered, i.e., that the director is confined everywhere to a single plane. The first assumption is approximately justified for common nematic mesogens; the second is reasonable since, as evidenced by Figs. 11(a) and 11(b), the patterned surface promotes variation in the polar coordinate only and places no restriction on the azimuthal orientation. Here the coordinate system is scaled by the thickness of the liquid crystal layer L_z, so that the periods of the pattern in the x and y directions, L_x and L_y, are dimensionless quantities.

Here, since $L_x \neq L_y$, we require a solution of the form

$$\theta(x,y,z) = \theta_0 + \sum_{n=-\infty}^{\infty}\sum_{m=-\infty}^{\infty} \frac{1}{\sqrt{L_x L_y}}\left(A_{nm}e^{-\nu_{nm}z} + B_{nm}e^{\nu_{nm}z}\right)\exp[i2\pi(nx/L_x + my/L_y)]. \tag{4}$$

The Euler-Lagrange equation [26]

$$(\tau\cos^2\phi + \sin^2\phi)\frac{\partial^2\theta}{\partial x^2} + (\tau\sin^2\phi + \cos^2\phi)\frac{\partial^2\theta}{\partial y^2} + (1-\tau)\sin(2\phi)\frac{\partial^2\theta}{\partial x\partial y} + \frac{\partial^2\theta}{\partial z^2} = 0 \tag{5}$$

is satisfied if the ν_{nm} are chosen:

$$\nu_{nm} = \frac{\pi}{L_x L_y}\sqrt{2(\tau+1)\left(L_x^2m^2 + L_y^2n^2\right) - 2(\tau-1)\left[2L_xL_ymn\sin(2\phi) + \cos(2\phi)\left(L_x^2m^2 - L_y^2n^2\right)\right]}. \tag{6}$$

The remaining coefficients are obtained from the weak anchoring boundary conditions, which for the harmonic anchoring potential

$$g_H(\theta,\theta_e) = \frac{W_\theta}{2}(\theta-\theta_e)^2 \tag{7}$$

are

$$\pm L_\theta\frac{\partial\theta}{\partial z} + \theta = \theta_e, \tag{8}$$

where $\theta_e(x,y)$ is the spatially varying easy axis promoted by the pattern, and the sign corresponds to the direction of the surface normal pointing out of the liquid crystal layer at the appropriate boundary and where the dimensionless parameter associated with polar anchoring L_θ is

$$L_\theta = \frac{K_1}{W_\theta L_z}. \tag{9}$$

As a guide to interpreting this number, for a cell thickness $L_z = 10\ \mu$m and typical unpatterned values of $W_\theta = 10^{-5}\mathrm{Jm}^{-2}$ and $K_1 \approx 10pN$ (5CB) the value of $L_\theta = 0.01$.

By inserting (4) into (8) and performing routine calculations, the coefficients θ_0, A_{nm}, and B_{nm} are obtained:

$$\theta_0 = \pi/4, \tag{10}$$

$$A_{nm} = \frac{e^{\nu_{nm}}c_{nm}}{L_\theta\nu_{nm}(e^{\nu_{nm}}-1) + (e^{\nu_{nm}}+1)},$$

$$B_{nm} = \frac{c_{nm}}{L_\theta\nu_{nm}(e^{\nu_{nm}}-1) + (e^{\nu_{nm}}+1)}, \tag{11}$$

where the c_{nm} are the Fourier coefficients of the easy axis profile $\theta_0(x,y)$ at the $z=0$ and $z=1$ surfaces, respectively:

$$c_{nm} = d_{nm} = \begin{cases} -\frac{\sqrt{L_xL_y}}{\pi nm} & n,m \text{ odd} \\ 0 & \text{otherwise} \end{cases}. \tag{12}$$

Having determined the solution as above, the free energy may be evaluated by inserting (4) into (3) and performing necessary integrations. The bulk energy is

$$F_b = \sum_{nm}\frac{\pi^2}{L_x^2L_y^2\nu_{nm}}\left[\left(A_{nm}^2e^{-\nu_{nm}} + B_{nm}^2e^{+\nu_{nm}}\right)\sinh(\nu_{nm}) + 2A_{nm}B_{nm}\nu_{nm}\right]\left\{(1+\tau)\left(L_x^2m^2 + L_y^2n^2\right) + (1-\tau)\times\left[\cos(2\phi)\left(L_x^2m^2 - L_y^2n^2\right) + 2L_xL_ymn\sin(2\phi)\right]\right\}$$

$$+\sum_{nm}\frac{1}{2}\nu_{nm}\left[\left(A_{nm}^2e^{-\nu_{nm}} + B_{nm}^2e^{+\nu_{nm}}\right)\sinh(\nu_{nm}) - 2A_{nm}B_{nm}\nu_{nm}\right]. \tag{13}$$

The surface energy (for each surface) is

$$F_s = \pi^2L_xL_y/16 + \frac{1}{L_\theta}\sum_{nm}(A_{nm}+B_{nm})\times(A_{nm}+B_{nm}-2c_{nm}). \tag{14}$$

The free energy per unit area as a function of ϕ is plotted in Fig. 12 for different values of L_θ and L_y/L_x with $\tau = 1/2$ and $L_x = 1$. For the strongest anchoring depicted, where $L_\theta = 0.05$, it is apparent that a very slight difference in L_x and L_y is sufficient to break the degeneracy of the configurations aligned along the x and y axes, respectively; once $L_y/L_x \gtrsim 1.5$ there is no stable state aligned along the x axis.

Rectangle-patterned surfaces are surfaces of adjustable azimuthal anchoring energy: they may be thought of as promoting an effective azimuthal anchoring potential [1], the strength of which is varied by modest changes in the aspect ratio of the rectangles. From the plot in Fig. 12(a), it is apparent that over the range of aspect ratios 1–2, the effective azimuthal anchoring energy varies by a factor of roughly 5. The controllability is, however, contingent on the ability of the pattern to deform the nematic as measured by the anchoring strength L_θ. Free energy profiles as a function of ϕ for increasing values of L_θ, corresponding to weaker anchoring, are displayed in Fig. 12(b)–12(f). As L_θ increases, the anchoring transition described in our previous paper [26] occurs [Fig. 12(c)] whereby the preferred azimuthal orientation, indicated by the position of the minimum, is no longer along the length or breadth of the square pattern, but lies roughly along the diagonal. For the largest value of $L_\theta = 0.2$ plotted, the depth of the effective azimuthal anchoring potential is significantly smaller than for the $L_\theta = 0.05$ case.

The variation of the preferred azimuthal orientation as a function of aspect ratio also depends strongly on the anchoring parameter around the anchoring transition as may be seen in Fig. 12(c)–12(e), while both the edge- [Fig. 12(a), 12(b)] and diagonally aligned states [Fig. 12(f)] are insensitive to the aspect ratio of the pattern. The experiment described in the previous section took place in this diagonal regime, and so the observed alignment angle as a function of aspect

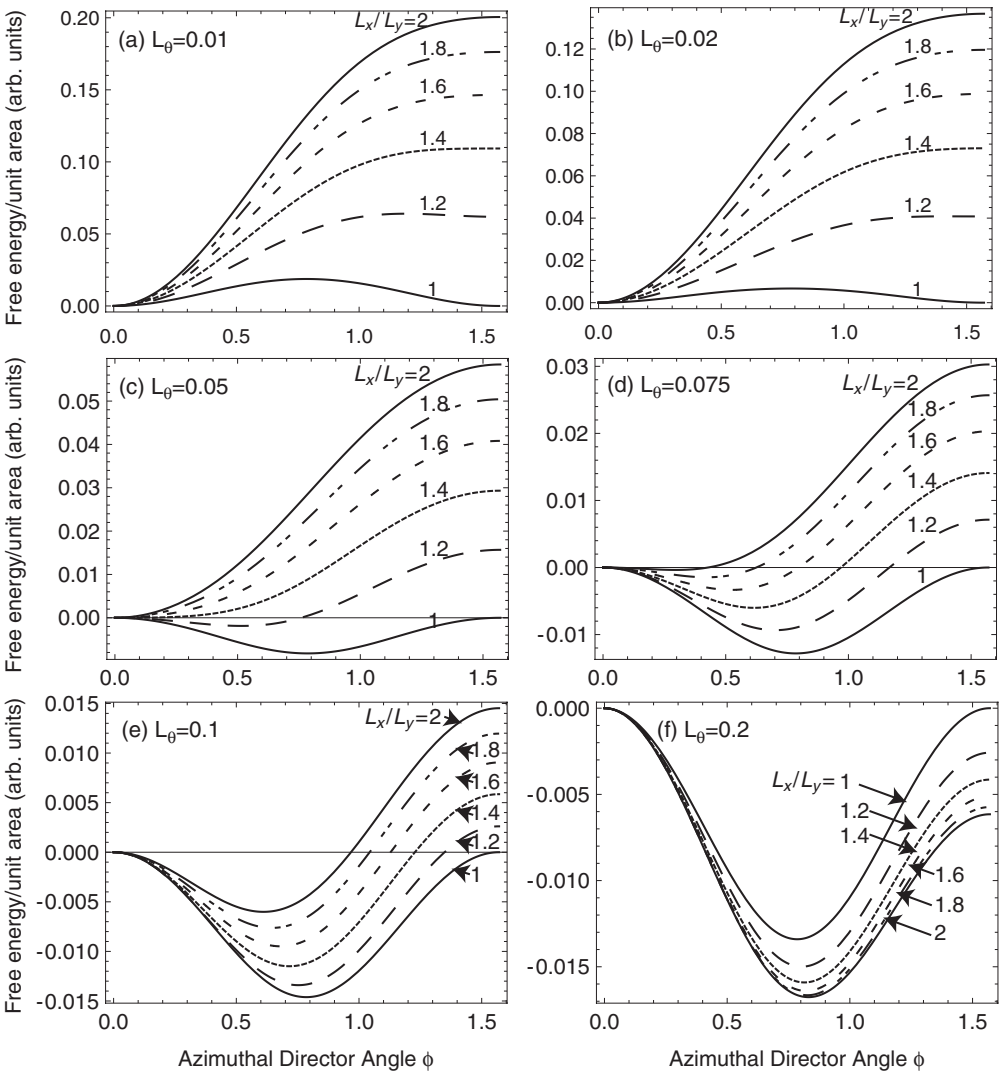

FIG. 12. Free energy per unit area as a function of ϕ, plotted for various values of L_y/L_x.

ratio can be used to estimate the anchoring parameter; from Table II we obtain a value of $L_\theta \sim 0.08$. Here, the apparent contradiction between the Monte Carlo and experimental results is resolved by the continuum prediction that there exist two different anchoring regimes characterized by the anchoring parameter L_θ; the MC simulations and experiment have illuminated the two regimes. In all models the tendency is for the director to align with the long axis of the rectangles.

VI. CONCLUSIONS

In this work a surface prepared with a chessboard-like pattern of alternating vertical and planar rectangles has been shown to azimuthally align an adjacent nematic liquid crystal. Moreover, control of the alignment easy axis has been demonstrated in both azimuthal and zenithal coordinates achieved by adjusting the design parameters of the pattern, i.e., the length scale, aspect ratio, and relative anchoring strength of the rectangles.

Monte Carlo simulations of hard particles predict that the preferred alignment direction is along the long edges of the rectangles and that only modest aspect ratios $\sim 2-3$ are required to break the bistable alignment previously observed in square-patterned systems [26]. Hence, rectangle patterns resemble the striped system extensively studied [21,23,24] except that the bulk alignment is a monodomain and no bridging behavior, where the nematic follows the pattern throughout the film, was observed; there is only weak modulation in the polar angle at the film center, in agreement with that predicted by continuum theory. Control of the tilt angle over a range of $\sim 20^\circ$–40° was observed by running a sequence of MC simulations and adjusting the relative anchoring strength of the vertical and planar regions. Simulations with increasing L_x/L_y had a distribution of particles increasingly strongly peaked around the alignment direction, suggesting that the azimuthal anchoring strength increases as a function of aspect ratio.

Experimental observations of a nematic aligned on rectangle surfaces prepared by chemical patterning reveal a different behavior to that seen in the Monte Carlo simulation: while for increasing aspect ratio the azimuthal alignment direction indeed becomes more oriented toward the long edge of the rectangles, the alignment direction is along the diagonals and not the edges.

The disparity is resolved by our continuum model which predicts an anchoring transition from diagonal to edge alignment if the anchoring parameter $L_\theta \lesssim 0.05$. The thin film, only a few particles thick, used in the MC simulation is inside the edge-aligned strong anchoring regime. By fitting the observed variation of the azimuthal anchoring direction as a function of aspect ratio, we infer that the experimental anchoring parameter was $L_\theta \sim 0.08$. The proximity of this value to the critical value $L_\theta \sim 0.05$ suggests that with a suitable choice of materials, cell thicknesses, and patterns, the transition ought to be observable in a future experiment.

The key parameter in these systems $L_\theta \sim 0.05$, introduced in Eq. (9), is simply the ratio of the bulk splay elasticity to the product of the unpatterned polar anchoring strength and the film thickness. Thus, it is apparent that the edge-aligned behavior observed in the MC simulation part of our study was *not* dictated by their small length scale, in fact, the small d of the simulated systems acted to promote the diagonal alignment regime. That the simulations remained firmly in the small $L_\theta \sim 0.05$ regime is, then, a consequence of the very high anchoring coefficients pertaining to all models described in terms of monodisperse anisotropic particles adsorbed at planar substrates.

Previous studies [30] have shown that the fine-tuning of surface anchoring, typically achieved by selection of materials and preparation conditions, is necessary to optimize the performance of advanced electro-optic devices. Patterned substrates of the type considered here, however, have the potential to offer a more convenient and well-controlled route to achieving such optimization, since all of the surface anchoring parameters, i.e., the easy axis, polar, and azimuthal anchoring energies, can be controlled by adjusting the design features of the pattern. In such systems, the emergent polar and azimuthal anchoring parameters can be viewed as resulting from a convolution of the basic material parameters and the imposed patterning. The conventional continuum description, thus, corresponds to an effective integration of a potential spectrum of various surface-printed features on length scales ranging from nanometers to microns.

ACKNOWLEDGMENTS

This work was supported by the Engineering and Physical Research Council, Grant No. GR/S59833/01. We acknowledge useful conversations with Chris Care, Tim Spencer, and Paulo Teixeira which have been beneficial to our understanding of the systems studied here. C.A.-D. and D.J.C. performed the MC simulations, J.P.B. performed the experiments with Jim Henderson and Stephen D. Evans, T.J.A. constructed the continuum theory; C.A.-D., D.J.C., and T.J.A. prepared the manuscript with advice from J.P.B.

[1] L. Harnau, S. Kondrat, and A. Poniewierski, Phys. Rev. E **76**, 051701 (2007).
[2] J. H. Kim, M. Yoneya, and H. Yokoyama, Nature (London) **420**, 159 (2002).
[3] F. K. Lee, B. Zhang, and P. Sheng, Appl. Phys. Lett. **85**, 5556 (2004).
[4] V. K. Gupta and N. L. Abbott, Langmuir **12**, 2587 (1996).
[5] V. K. Gupta and N. L. Abbott, Science **276**, 1533 (1997).
[6] Y. L. Cheng, D. N. Batchelder, S. D. Evans, J. R. Henderson, J. E. Lydon, and S. D. Ogier, Liq. Cryst. **27**, 1267 (2000).
[7] I. H. Bechtold and E. A. Oliveira, Liq. Cryst. **32**, 343 (2005).
[8] I. H. Bechtold and E. A. Oliveira, Mol. Cryst. Liq. Cryst. **442**, 41 (2005).
[9] M. Schadt, K. Schmitt, and V. Kozinkov, Jpn. J. Appl. Phys. **31**, 2155 (1992).
[10] M. Stalder and M. Schadt, Liq. Cryst. **30**, 285 (2003).
[11] B.-w. Lee and N. A. Clark, Science **291**, 2576 (2001).
[12] Y. Yi, V. Khire, C. Bowman, J. Maclennan, and N. Clark, Jpn. J. Appl. Phys. **103**, 093518 (2008).
[13] J. H. Kim, M. Yoneya, J. Yamamoto, and H. Yokoyama, Appl. Phys. Lett. **78**, 3055 (2001).
[14] M. Yoneya, J. H. Kim, and H. Yokoyama, Appl. Phys. Lett. **80**, 374 (2002).
[15] C. V. Brown, M. J. Towler, V. C. Hui, and G. P. Bryan-Brown, Liq. Cryst. **27**, 233 (2000).
[16] G. P. Bryan Brown, E. L. Wood, C. V. Brown, J. C. Jones, I. C. Sage, and P. Brett, SID Sym. **28**, 37 (1997).
[17] J. H. Kim, M. Yoneya, and H. Yokoyama, Appl. Phys. Lett. **83**, 3602 (2003).
[18] S. Kitson and A. Geisow, Appl. Phys. Lett. **80**, 3635 (2002).
[19] L. Cattaneo, P. H. J. Kouwer, A. E. Rowan, and Th. Rasing, Jpn. J. Appl. Phys. **113**, 014503 (2013).
[20] G. Barbero, T. Beica, A. L. Alexe-Ionescu, and R. Moldovan, J. Phys. II France **2**, 2011 (1992).
[21] T. J. Atherton and J. R. Sambles, Phys. Rev. E **74**, 022701 (2006).
[22] J. P. Bramble, S. D. Evans, J. R. Henderson, C. Anquetil, D. J. Cleaver, and N. J. Smith, Liq. Cryst. **34**, 1059 (2007).
[23] C. Anquetil-Deck and D. J. Cleaver, Phys. Rev. E **82**, 031709 (2010).
[24] T. J. Atherton, Liq. Cryst. **37**, 1225 (2010).
[25] S. Kondrat, A. Poniewierski, and L. Harnau, Eur. Phys. J. E **10**, 163 (2003).
[26] C. Anquetil-Deck, D. J. Cleaver, and T. J. Atherton, arXiv:1207.1731v1 (2012).
[27] P. Padilla and E. Velasco, J. Chem. Phys. **106**, 10299 (1997).
[28] J. G. Gay and B. J. Berne, J. Chem. Phys. **74**, 3316 (1981).
[29] D. J. Cleaver and P. I. C. Teixeira, Chem. Phys. Lett. **338**, 1 (2001).
[30] T. J. Spencer and C. M. Care, Phys. Rev. E **74**, 061708 (2006).